Contents lists available at ScienceDirect

Materials Science and Engineering B

Design of linear shaped thermoelectric generator and self-integration using shape memory alloy

Hee Seok Kim [a],[1], Takashi Itoh [b], Tsutomu Iida [c], Minoru Taya [a],[*], Keiko Kikuchi [d]

[a] *Center for Intelligent Materials and Systems, Department of Mechanical Engineering, University of Washington, Box 352600, Seattle, WA 98195-2600, USA*
[b] *EcoTopia Science Institute, Nagoya University, Furo-cho, Chikusa-ku, Nagoya 464-8603, Japan*
[c] *Department of Materials Science and Technology, Tokyo University of Science, 2641 Yamazaki, Noda-Shi, Chiba 278-8510, Japan*
[d] *Department of Materials Processing, Tohoku University, Sendai, 980-8579, Japan*

A B S T R A C T

A segmented linear-shaped thermoelectric generator was designed with n-type Mg$_2$Si and p-type higher manganese silicide as higher temperature segments and n-type and p-type Bi–Te based compounds as low temperature legs. A new design of a dovetail-shaped AlN–Cu composite as an electrode enabled linear-shaped thermoelectric generator to be securely bonded to the combustion chamber walls by using shrink-fit-joining method. As-assembled linear thermoelectric generator is lighter in generating more power output as compared with conventional π-shaped thermoelectric generator. The linear thermoelectric module generates the output power of 0.513 W under 500 °C temperature difference and the specific power density was measured at 89.3 W/kg, the output power was improved by 7% and the specific power density more than 2 times, as compared with those of the π-shaped thermoelectric module based on the same set of thermoelectric materials and temperature differential.

Crown Copyright © 2013 Published by Elsevier B.V. All rights reserved.

1. Introduction

Thermoelectric (TE) devices have been used in a wide range of applications for energy harvesting systems by converting thermal energy directly to electrical energy [1–4]. The performance of TE materials is determined by the dimensionless figure of merit (ZT) which is defined as,

$$ZT = \frac{S^2\sigma}{\kappa}T \tag{1}$$

where S, σ, κ and T are the Seebeck coefficient, electrical conductivity, thermal conductivity and the absolute temperature at which the properties are measured, respectively. Recently, energy harvesting devices using TE generator (TEG) modules have been applied to airborne applications [5,6] to increase fuel efficiency by recapturing wasted exhaust heat and converting it to useable electricity [7].

The conventional TEG is single-stage couples connecting electrically in series and thermally in parallel with π-shape design. A typical π-shaped TEG is made by connecting N pairs of n-type and p-type TE legs, which gives rise to the output voltage proportional

to N. To design higher power output, Harman [8] suggested the cascaded design of stacking two or more π-shaped TEGs. TE module at lower legs consisting of TE materials working best for low temperature range generates power from the heat rejected by the upper module based on TE legs operating at high temperature. This design has a disadvantage for weight sensitive applications because extra ceramic substrates and metal electrodes increase the total weight of the device. One way to improve the TE performance as well as to minimize the total weight of the device is the segmented design by dividing the n-type and p-type legs into several segments using different TE materials [9,10]. However, the π-shaped planar structure becomes unstable if the length of n-type and p-type TE column is not identical, which makes the TEG module weak at high temperature environment. Stockholm [11] introduced a linear design concept of TE module where an electric current flows in a straight line through the TE legs while the electric current in the π-shaped TEG design flows alternatively up and down. Crane and Bell [12] showed the aspect ratio of n-type in the linear TEG design can be controlled with that of p-type independently. Sakamoto et al. [13] designed a linear-shaped TEG for high temperature range by using only n-type TE element, which has a limit of scaling up by connecting a number of n-type uni-legs electrically in series and thermally in parallel. However, the reported TEGs used bulk Cu or stainless steel as electrodes, which are the main source of increasing the total device's weight. In addition, ceramic substrates on top and bottom sides of the module are still required to avoid short-circuiting.

In this study, an advanced design of the segmented linear TEG is proposed for its integration into the walls of a combustion engine system in unmanned aerial vehicles (UAV) with two innovative designs: (a) dovetail-shaped electrode based on a composite of copper (Cu) and aluminum nitride (AlN), and (b) self-jointing by shrink-fit behavior of Fe-based shape memory alloy (Fe-SMA). As the high temperature TE segments, bulk Mg_2Si of n-type and higher manganese silicide (HMS, $MnSi_{2-x}$, $x = 0.250–0.273$) of p-type are used since they are light-weight, non-toxic and low-cost TE compounds working for high temperature range. In the following, we will discuss linear-shaped TEG design and also its performance as compared with π-shaped TE module.

2. Preparation of TE segments

For accurate comparison with the π-shaped segmented TEG reported by Kim [14], the same set of TE segments are used to assemble linear-shaped TEG in this study. All TE legs in linear-shaped TEG were synthesized and prepared from the same TE materials used in the π-shaped TEG so that the measured TE properties of each segment in our previous study can be utilized to predict the performance of π-shaped and linear-shaped TEGs. The following states briefly the preparation of TE segments.

Bi doped Mg_2Si was fabricated as n-type segment on the high temperature side. Mg (99.95%), Si (99.9999%) and Bi (99.999%) were prepared with Mg:Si ratio of 67:33 (at%) including the Bi dopant (3 at%) and polycrystalline Mg_2Si was synthesized by an electric furnace [15]. The obtained ingot was ground into powder using planetary ball milling technique, and the powder was transferred to a glove box with Ar atmosphere to set up in a graphite die for spark plasma sintering (SPS) (Sumitomo Coal Mining Co., Ltd., Dr. Sinter 1020S). The assembled set of graphite die and punches was heated in a two-step procedure of SPS, where the first pre-heating step allows one to maintain low vacuum level by holding

the temperature at 500 °C with the pressure of 30 MPa. For the second step, the graphite set was pressurized up to 50 MPa while it was heated to 750 °C and kept for 3 min with a heating rate of 100 °C/min [14]. The sintered Mg_2Si pellet of 15 mm diameter was cut into rectangular pillars of 4 mm × 4 mm × 5 mm by a diamond saw.

To fabricate p-type HMS segment which is for the high temperature leg, Mn (99.9%) and Si (99.9%) were individually put into an alumina jar with alumina balls, and mechanical grinding was carried out in vibration ball milling equipment for 10 h in Ar atmosphere, where the ball to powder volume ratio was 20:1 [16]. The ground powders were blended with Mn:Si ratio of 35.5:64.5 (at%) in a rotary mixer at 100 rpm for 1 h in Ar atmosphere, then the mixed powders were transferred into the graphite mold of 20 mm diameter [16]. The HMS disk was sintered by SPS process at 900 °C and 30 MPa for 15 min in a vacuum. As-sintered HMS was diced into 4 mm × 4 mm × 3.4 mm by a diamond saw.

As TE segments for low temperature legs, both n-type and p-type Bi-Te based compounds were purchased from Tellurex Inc. in the shape of 4 mm × 4 mm × 1 mm and 4 mm × 4 mm × 2.6 mm, respectively.

TE properties of all TE segments were evaluated. The Seebeck coefficient (S) and electrical conductivity (σ) were measured as a function of temperature using Ulvac-Rico, ZEM-3 with the bar sample in size of 2 mm × 2 mm × 10 mm. The thermal conductivity (κ) a disk sample of 1 mm thickness and 10 mm diameter was measured as a function of temperature by using a laser flash system (Ulvac-Rico, TC-9000). The measurements of TE properties of Bi-Te alloys were carried out over the temperature range from room temperature to 300 °C while those of Mg–Si and HMS from room temperature up to 600 °C. Fig. 1 shows the temperature dependent TE properties, where p-type Bi–Te, n-type Mg–Si and p-type HMS were the average values based on the five independent measurements shown as error bars in Fig. 1(a–d) by the above measurement
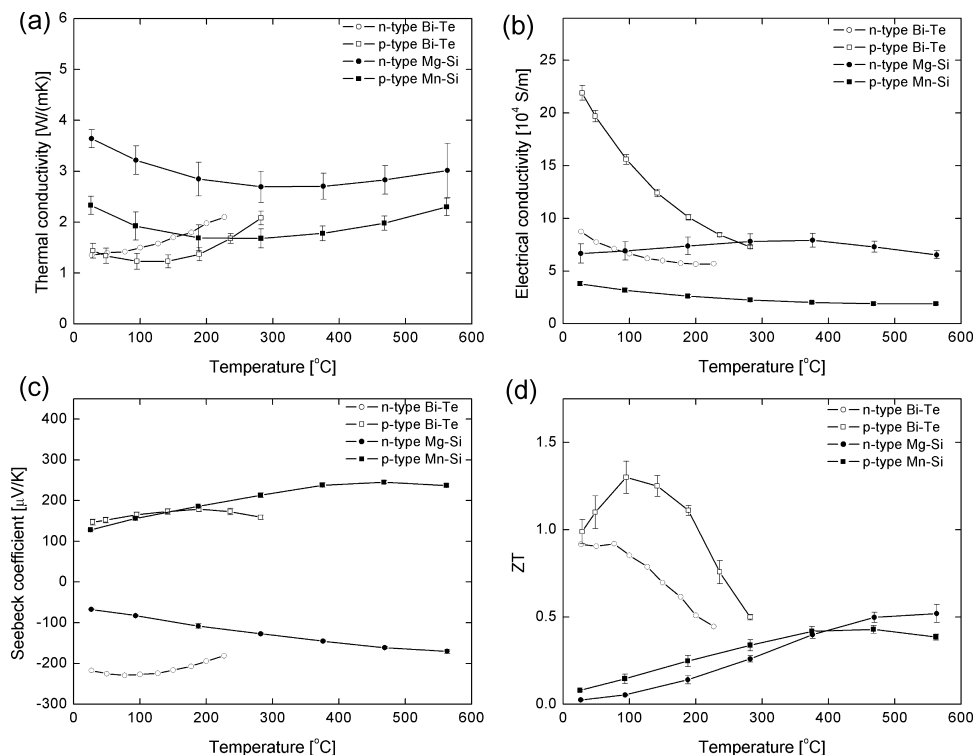

Fig. 1. Temperature dependent TE properties of n-type Mg_2Si and p-type HMS as high temperature segment, and n-type Bi–Te–Se and p-type Bi–Sb–Te as low temperature segment, in which the same set of TE segments are utilized in the work of Kim [14]: (a) thermal conductivity, (b) electrical conductivity, (c) Seebeck coefficient, and (d) dimensionless the figure of merit, ZT.
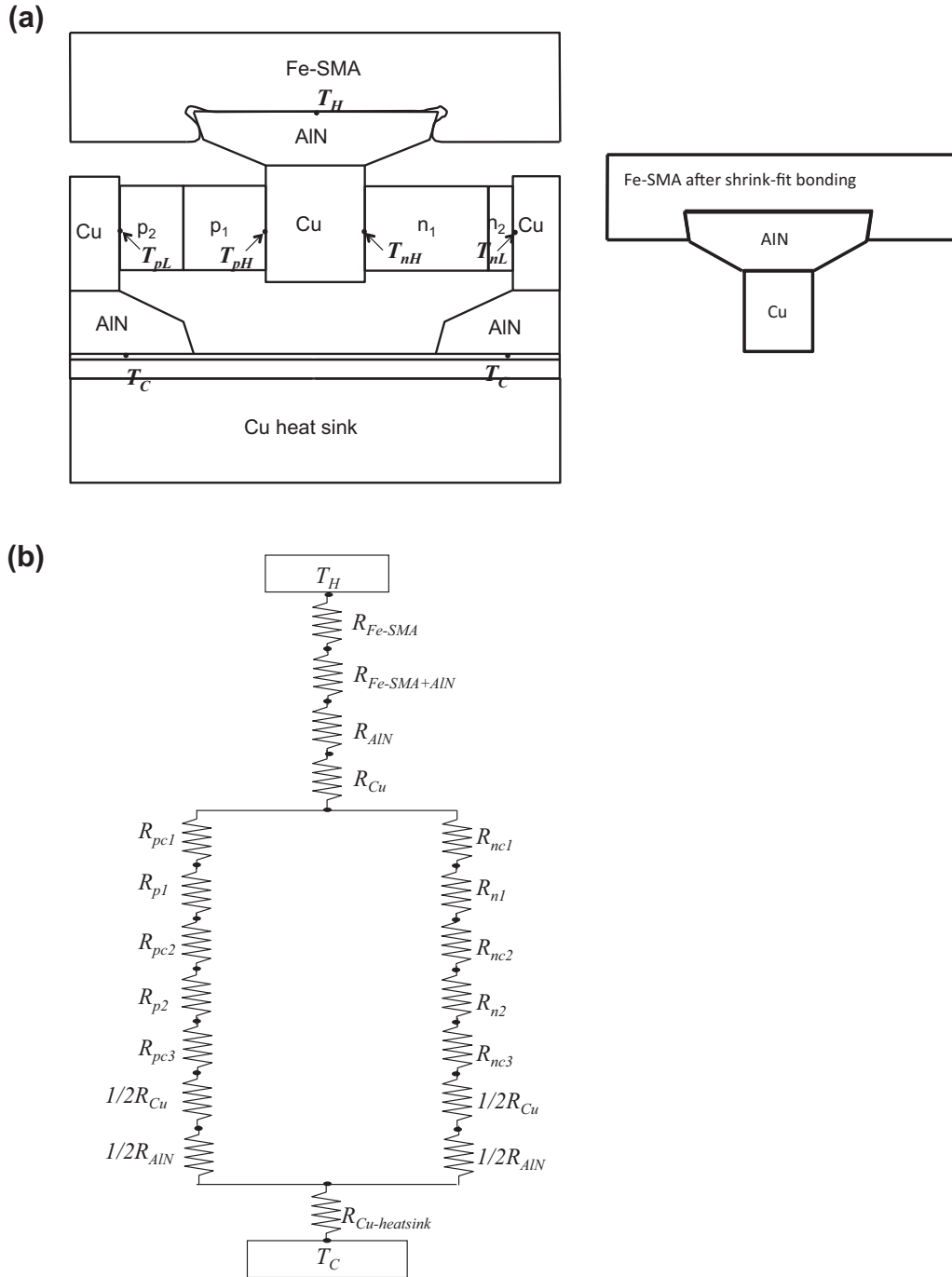
Fig. 2. (a) Schematic figure of the assembled linear-shaped TE module showing full and half shape of AlN–Cu electrodes (left), and the completion of shrink-fit by increasing temperature above T_{Af} of Fe-SMA (right), and (b) thermal resistor network model corresponding to (a).

equipments while TE properties of n-type Bi–Te was measured by Tellurex Inc., thus their values are based on single value provided by the company.

The temperatures at the bonding interfaces of the n_1–n_2 in n-type and the p_1–p_2 in p-type columns were determined by intersecting the ZT–temperature curves of the low temperature TE materials (n_2, p_2) and those of the high temperature TE materials (n_1, p_1), where n and p denote n-type and p-type, and subscripts 1 and 2 indicate high temperature TE segment and low temperature TE segment, respectively, see Fig. 2(a). The desired temperatures at the interfaces are 200 °C at the n-type junction and 300 °C at the p-type junction under the boundary condition at $\Delta T = 500$ °C. Lengths of all segments are optimized based on the analytical study based

on the heat conduction law of 1-D model. The combined n-type column consists of 5 mm of Mg_2Si and 1 mm of Bi–Te–Se while the p-type leg is composed of 3.4 mm of HMS and 2.6 mm of Bi–Sb–Te.

3. Linear-shaped TEG fabrication

3.1. Dovetail-shaped electrode

Conventional electrodes in the linear TE design [12,13,17] were made by bulky T-shaped metals of Cu or stainless steel, where lower vertical block was only incorporated to pass electric current in a horizontal direction while the top horizontal portion of the T-shaped electrode played a role of absorbing heat energy from a heat
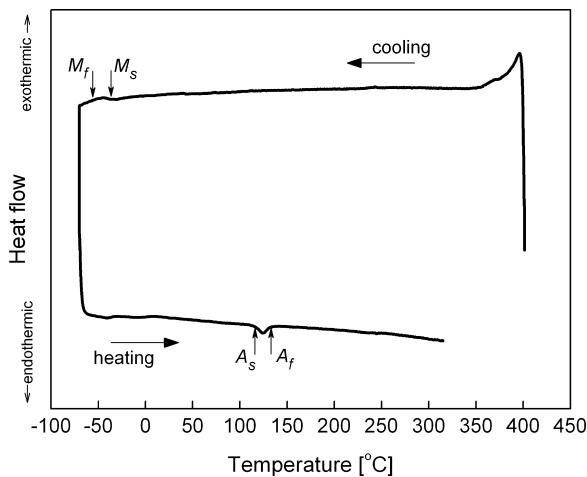
Fig. 3. DSC chart showing T_{Ms}, T_{Mf}, T_{As}, and T_{Af}.

source. The new concept of a dovetail-shaped composite electrode proposed in this study is to replace the top part of the metal block with AlN ceramic material which transfers heat from a heat source effectively to lower Cu part of the T-shape electrode while preventing a short circuit between adjacent n–p pairs, see Fig. 2(a), for AlN is thermally conductor, but insulator electrically. AlN and Cu were brazed by using Ag based brazing filler (Ag–Cu–Ti) at 800 °C. AlN has much lower mass density (3.26 g/cm^3) than copper (8.94 g/cm^3) and stainless steel (8.03 g/cm^3) so that the total weight of fully assembled linear TEG using the composite electrodes becomes lighter than that of conventional linear TEGs. Another feature of the proposed AlN–Cu electrode has an angle in upper AlN part. In Fig. 2(a), the upper angled edge of AlN cooperates in a shrink-fitting assembly to be integrated into a combustion chamber's wall made of Fe based SMA (Fe-SMA). AlN–Cu electrodes in a half shape are required for the complete TE module assembly, which are placed at the far ends of right and left sides. A compressive force is applied horizontally on the flat end of the half shape electrodes is important for the compressive force to be applied horizontally so that both thermal and electrical resistances at the interfaces can be minimized and heat flows to the cold side of the TEG, the bottom Cu heat sink shown in Fig. 2(a). The thermal resistor network model of the linear TEG was constructed as shown in Fig. 2(b), which will be discussed in Section 5.

3.2. Fe-SMA for the shrink-fit integration

The concept of new integration method is that the AlN part of the dovetail-shaped electrode is inserted into the groove of the combustion chamber's wall which is made of low-cost Fe–Si–Mn–Cr SMA (Fe-SMA) [18]. As-received Fe-SMA plate from the supplier (Awaji Materia Co., Ltd., Japan) was characterized to examine the transformation temperatures; martensite start temperature (T_{Ms}), martensite finish temperature (T_{Mf}), austenite start temperature (T_{As}), and austenite finish temperature (T_{Af}) by differential scanning calorimeter (DSC) from −70 °C to 400 °C, which was measured under no applied stress, so the transformation was not stress induced. Fig. 3 is the DSC results of this Fe-SMA showing the weak peaks as compared with TiNi-SMA. From the DSC results the endothermic peak was observed around 125 °C on the heating curve, where T_{As} and T_{Af} were found as 115 °C and 135 °C, respectively. The exothermic peak on the cooling path was detected around at −50 °C but T_{Ms} and T_{Mf} were not clearly shown. Since the transformation to the martensite phase occurs much below room temperature, Fe-SMA after the shrink-fit assembly by heating above T_{Af} and cooling down to room temperature is still the

austenite phase, which means no phase transition occurs at the operation temperature range of TEG, room temperature to 500 °C.

In order to obtain the correct shape memory strain during the shrink-fit joining of the dovetail-shaped electrode and Fe-SMA plate, 6% tensile strain was applied to as-received Fe-SMA plate. This prestraining was repeated again to secure larger recovery strain of up to 3.5%. Then, the prestrained Fe-SMA plate is subjected to shape memorization process, i.e., annealing at 600 °C for 2 h with the heating rate of 10 °C/min under the gas flowing (1 L/min) environment of 95% Ar and 5% hydrogen, then it was cooled down to room temperature. Then, the Fe-SMA was machined with groove, followed by insertion of the top AlN part of the dovetail-shaped electrodes into the grooves of the Fe-SMA plate. Heating up to temperature above T_{Af} led to a shrink-fit assembly of the dovetail-shaped AlN–Cu electrodes into Fe-SMA plate, as shown on the right-hand side figure in Fig. 2(a). The compressive strain of Fe-SMA plate for the shrink-fit joining can be optimized by changing the length of the groove. To this end, various shrink-fit strains were applied such as 0.1%, 0.3%, 0.5%, 1% and 2% compression. If the shrink-fit strain is not optimized, cracks could occur at the end of shrink-fit assembly, for example the use of larger than 0.3% compression led to such cracking emanating from the sharp corners of the groove. It was found that 0.1% of the fitting strain enables the assembly to be crack free, where the corner ends of the machined groove were rounded to avoid the stress concentration due to the sharp corner of AlN parts. This shrink-fit bonding is expected to be much more durable compared to solder based bonding which is prone to failure due to the vibration-induced cracking soldered region.

3.3. Two-pair TEG fabrication and the output power measurement

The high temperature TE legs made of Mg$_2$Si and HMS were brazed to a Cu block of the dovetail-shaped at 680 °C for 5 min using Ag–Cu–Sn–Zn soldering materials. The pre-assembled parts were inserted into the grooves of Fe-SMA plate, and then the shrink-fitting was carried out at 350 °C for 30 min with the heating rate of 10 °C/min. After cooling down to room temperature naturally, soldering was achieved between the low temperature TE segments (n$_2$, p$_2$) and the high temperature TE legs (n$_1$, p$_1$) under applied compression, and the half shape of Cu–AlN electrodes were also soldered to n$_2$ and p$_2$ legs using Pb–Ag–Sn–In soldering materials at 350 °C for 5 min. It is essential that Ti (50 nm) and Ag (1 μm) layers were thinly pre-coated on the bonding surfaces of each TE segment prior to the soldering since Ti is an ideal adhesion material, and Ag has low wetting contact angle, which ensures lower contact resistance and strong bonding. All brazing and soldering processes were carried out under the gas flowing (2 L/min) environment of 95% Ar and 5% hydrogen to prevent joint interfaces from being oxidized and contaminated during the high temperature bonding process.

It is highly desired to minimize the electrical contact resistances of linear TE legs since the larger contact resistance degrades TEG's performance by reducing its output power generation [19]. The voltage drops across the bonding interfaces were measured using a four-point probe method, and the electric contact resistance is obtained from ohm's law. The measured contact resistances at the interface of Cu electrode bonded with n-type and p-type TE segments are 3.2 μΩ cm^2 and 52.8 μΩ cm^2 at high temperature side, and 28.8 μΩ cm^2 and 59.2 μΩ cm^2 at low temperature side, respectively.

A compression loading by bolt-joining was applied horizontally the linear TEG where thin AlN plates were inserted between the half shape electrodes and side supports of the bottom Cu jig to avoid a short circuit. This pre-assembled part was inserted between a solid Cu heat sink with a water flow channel inside and a heat
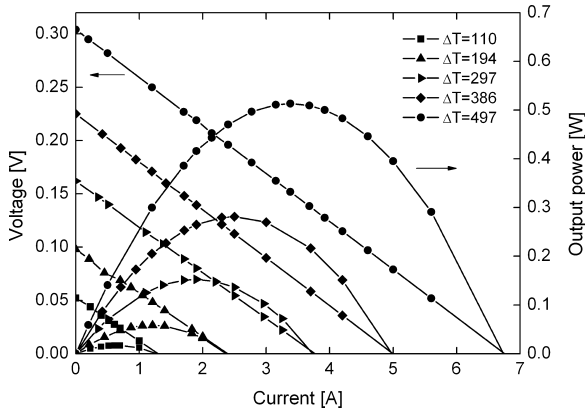
Fig. 4. The experimental results of two-pair linear TEG test: *I–V* curve and output power generation as a function of load current with various ΔT.

source made of two cartridge heaters, where the heat source is not shown in Fig. 2(a). This assembly was insulated by 2-in. thick fiberboard to ensure 1-D heat flow vertically while the electric current flowed horizontally, and thermocouples were installed at each bonding interface to monitor temperatures. The output power was measured under the temperature difference ($\Delta T = T_H - T_C$) varied as high as $\Delta T = 500\,°C$, where the hot side temperature (T_H) at the AlN part of dovetail-shaped electrode was set to 523 °C while the cold side temperature (T_C) of the bottom AlN at the half shape of Cu–AlN electrode was maintained as low as 26 °C. Fig. 4 shows the results of the output power generated by the linear TEG at various ΔTs. The maximum output power measured at $\Delta T = 497\,°C$ is 0.513 W at a load current of 3.38 A under a resistance of 45 mΩ. The specific power density was calculated to be 89.2 W/kg by dividing the output power by the total weight of the two-pair linear-shaped TEG excluding Fe-SMA plate, which is 5.75 g.

4. Comparison of experimental data with predictions by the model

The works of Swanson et al. [20], and El-Genk et al. [21,22] have constructed the generalized analytical model to estimate output power generated by the segmented π-shaped TEG. By expanding the model of Min and Rowe [23], a model incorporating the effect of the ceramic substrate, electrical contacts at the interface of TE segments, and metal electrodes was reported by Kim [14]. From this model, the load voltage is,

$$V = -\left[\frac{2}{A}\left(\sum_{i=1}^{2}\rho_{p_i}L_{p_i} + \sum_{i=1}^{3}\rho_{pc_i} + \sum_{i=1}^{2}\rho_{n_i}L_{n_i} + \sum_{i=1}^{3}\rho_{nc_i}\right) + R_w\right]I + V_{OC} \tag{1}$$

ΔT_{sub_H}, ρ_{n_i}, ρ_{pc_i} and ρ_{nc_i} are electrical resistivity of p-type and n-type element and contact resistance between ith and $(i+1)$th of p-type and n-type elements, respectively. L_{sub_H} and L_{n_i} are the length of each ith p-type and n-type segment, and V_{OC} is open circuit voltage. R_w is the electric resistance of lead wires measured experimentally.

The output power of two pairs in the linear-shaped TEG is,

$$P = \frac{2(S_p^M - S_n^M)^2(T_H - T_C)^2}{\left[1/A\left(\sum_{i=1}^{2}\rho_{p_i}L_{p_i} + \sum_{i=1}^{3}\rho_{pc_i} + \sum_{i=1}^{2}\rho_{n_i}L_{n_i} + \sum_{i=1}^{3}\rho_{nc_i}\right) + R_w/2\right]} \cdot \frac{m}{(1+m)^2} \tag{2}$$

where m is defined as R_L/R. S_p^M and S_n^M are the effective Seebeck coefficient. The explicit expressions of κ_{sub_H} and S_n^M are,

$$S_p^M = \frac{\sum_{i=1}^{2}S_{p_i}(\kappa_p^E L_{p_i})/(\kappa_{p_i}L_p)}{\sum_{i=1}^{2}S_{p_i}(\kappa_p^E L_{p_i})/(\kappa_{p_i}L_p) + (\kappa_p^E L_{sub_H})/(\kappa_{sub_H}L_p) + (\kappa_p^E L_{sub_C})/(\kappa_{sub_C}L_p)},$$

$$S_n^M = \frac{\sum_{i=1}^{2}S_{n_i}(\kappa_n^E L_{n_i})/(\kappa_{n_i}L_n)}{\sum_{i=1}^{2}S_{p_i}(\kappa_n^E L_{n_i})/(\kappa_{n_i}L_n) + (\kappa_n^E L_{sub_H})/(\kappa_{sub_H}L_n) + (\kappa_n^E L_{sub_C})/(\kappa_{sub_C}L_n)}$$

κ_p^E and κ_{p_i} are effective thermal conductivity of all combined p-type leg and thermal conductivity of ith segment, respectively. L_p and L_n are total length of each combined leg. κ_{sub_H}, L_{sub_H} and ΔT_{sub_H} are the effective thermal conductivity, length, and temperature drop of the combined layer consisting of Fe-SMA plate, shrink-fit joint layer, and dovetail-shaped electrode at high temperature, respectively. κ_{sub_C}, L_{sub_C} and ΔT_{sub_C} are the same as the above at low temperature. ΔT_p and ΔT_{p_i} are the temperature difference through the combined p-type column and the temperature difference across ith segment of p-type, respectively.

The efficiency of the linear-shaped TEG is,

$$\eta = \frac{T_H - T_C}{T_H}\left\{\frac{4}{Z^M T_H} + \frac{2(S_{p_1}T_{p_1} - S_{n_1}T_{n_1})}{(S_p^M - S_n^M)T_H} - \frac{(R_{p_1} + R_{n_1})(T_H - T_C)}{2R_{tot}^M T_H}\right\}^{-1} \tag{3}$$

where R_{tot}^M is effective electrical resistance of 1-pair,

$$R_{tot}^M = \frac{1}{A}\left(\sum_{i=1}^{2}\rho_{p_i}L_{p_i} + \sum_{i=1}^{3}\rho_{pc_i} + \sum_{i=1}^{2}\rho_{n_i}L_{n_i} + \sum_{i=1}^{3}\rho_{nc_i}\right) + \frac{R_w}{2}$$

K_p^M and K_n^M are effective thermal conductance of p-type and n-type legs respectively.

$$K_p^M = \frac{K_p^E}{\sum_{i=1}^{2}(\kappa_p^E L_{p_i})/(\kappa_{p_i}L_p) + (\kappa_p^E L_{sub_H})/(\kappa_{sub_H}L_p) + (\kappa_p^E L_{sub_C})/(\kappa_{sub_C}L_p)},$$

$$K_n^M = \frac{\sum_{i=1}^{2}K_n^E}{\sum_{i=1}^{2}(\kappa_n^E L_{n_i})/(\kappa_{n_i}L_n) + (\kappa_n^E L_{sub_H})/(\kappa_{sub_H}L_n) + (\kappa_n^E L_{sub_C})/(\kappa_{sub_C}L_n)}$$

and, Z^M is module figure of merit which is defined as,

$$Z^M = \frac{(S_p^M - S_n^M)}{R_{tot}^M(K_p^M + K_n^M)}$$

Fig. 5 shows the measured and predicted curves under $\Delta T = 497\,°C$. The solid lines are the calculated predictions based on Eqs. (1) and (2), and the plotted markers are the measured data by experiment. In Fig. 5(a), the measured V_{OC} is 304 mV and the predicted value is 314 mV, which is in a good agreement within 3% difference. The maximum power output, 0.513 W is measured at the load resistance of 44.9 mΩ while the maximum output power by the analytical model is 0.517 W. This measured value and the theoretical calculation for output power generation are in a good agreement within 1% difference. Fig. 5(b) shows the maximum output power and efficiency as a function of ΔT (=$T_H - T_C$). The generated power is parabolic functions of ΔT and the measured value is in agreement with the predicted power equation, Eq. (2) when $m = 1$ for the impedance matching. The maximum module efficiency is 3.6% measured at $\Delta T = 497\,°C$ and the predicted value by Eq. (3) is 4.3%. A good agreement between the measured output power and predictions by the model indicates that the segmented linear-shaped TEG fabrication and its measurement processes were carried out correctly. However, there are larger differences from 17 to 32% between the measured efficiency and predictions. This shows that a perfect thermal management during the measurement is difficult even though an intensive insulation was applied for 1-D heat flow. This is mainly because of heat losses by convection
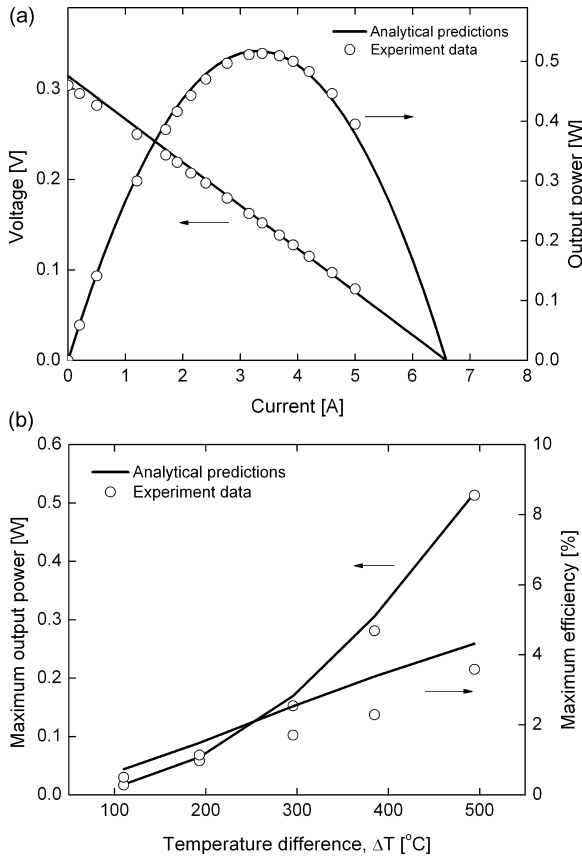
Fig. 5. Comparison of experimental data with prediction by the model: (a) I–V curve and output power as a function of load current, (b) the maximum output power and module efficiency as a function of ΔT.

and radiation. For a following research, the experimental measurement should be conducted at vacuum environment to avoid parasitic heat losses, which gives rise to more accurate results of efficiency measurement.

5. Discussion

Fig. 6 shows the comparison between measured data of the typical π-shaped TEG [14] and the linear-shaped TEG proposed in this study, where the same TE materials with the same dimension are used. The solid lines in Fig. 6(a) show the temperature difference only through TE segments as a function ΔT, where ΔT_n and ΔT_p are the measured temperature gap across the combined n-type and p-type column, respectively. The marker in square indicates n-type and that in circle is p-type, and the solid and hollow markers mean the linear TEG and π-shaped TEG data, respectively. The dotted line is the measured V_{OC}, where the solid and hollow triangles indicate the linear TEG and the π-shaped TEG. It is noted in Fig. 6(b) that the larger temperature gradient through TE legs in the linear design was induced than that in π-shaped TEG. This is mainly because of the reduced thermal resistance thank to the use of AlN–Cu composite electrode and shrink-fit integration method in the linear TEG design. Fig. 6(b) shows the measured temperature values (solid markers) when ΔT is 500 °C, and the numerical results by ANSYS (hollow markers with a cross symbol) and thermal resistor network model (hollow makers). The conditions used for the FEM thermal analysis based on ANSYS are as follows: (1) element type: plane55, (2) mesh size: 0.25 mm square, and (3) temperature boundary conditions: $T_H = 525$ °C and $T_C = 25$ °C for $\Delta T = 500$ °C. The ceramic materials covering TEG set for insulation and the space filled with air between the top Fe-SMA plate and the bottom Cu

block were taken into account for the accurate thermal analysis. In Fig. 6(b), the solid and dashed lines denoting the temperatures of given positions defined in Fig. 2(a) are for the linear TEG and π-shaped TEG, respectively. In addition, the thermal resistor network model of 1-D heat flow was built as shown in Fig. 2(b), which is corresponding to Fig. 2(a). The temperature at the nodes were calculated by using Kirchhoff's rule of $\sum Q_i = 0$ at each node i, where the heat flow $Q = \Delta T/R$ [24]. By applying for all nodes, the matrix form of $[Q] = [1/R][T]$ is obtained, and the temperatures at various nodes are calculated by taking the inverse of the matrix $[1/R]$. The thermal resistance R is defined as $R = \Delta x/(\kappa A)$, where κ, Δx, and A are thermal conductivity, thickness and cross-section area along with the heat flow, respectively. ΔT_n by experiment, thermal resistor model and ANSYS are 455 °C, 475 °C and 478 °C, and ΔT_p are 465 °C, 479 °C and 483 °C, respectively. These measured values and the predictions by FEM and the thermal resistor network model are in good agreement within 5% difference in ΔT_n and within 4% difference in ΔT_p. The temperature drops of the linear TE module from the dovetailed AlN to TE legs on both high and low temperature ends are smaller than those of the π TEG, which verifies that the thermal resistance through substrate layers in the linear TE design is smaller than that of π TEG, resulting in the larger temperature gradient in the linear TEG. This larger temperature gradient in the linear TEG generates larger electric potential, as shown by the dotted line in Fig. 6(a), which produces more output power generation, as shown in Fig. 6(c), where the I–V and I–P curves of the two different TEG designs under $\Delta T = 500$ °C are given. Thus, the maximum output power of the linear TEG design is higher by 7% more than that of the π TEG. Fig. 6(d) shows the generated output power and the specific power density as a function of ΔT, where the specific power density is defined as a power generation per a unit weight, i.e., in unit of W/kg. The dotted and solid lines show the calculated maximum out power and specific power density, respectively, and the solid and hollow markers are the experimental data of linear and π-shaped TEG, respectively. The advantage of the linear design in this study is to reduce the total weight of the TEG since the use of AlN plates and metal electrodes in the π-shaped TEG design is replaced by Cu–AlN T-shaped electrode. The specific power density of the linear TEG design is improved by 108% as compared with that of the π TEG for the weight of the linear TEG is 5.75 g while that of π-shaped TEG is 11.19 g where the both designs exclude the weight of the combustion chamber wall (Fe-SMA plate). The lighter weight is a critical issue in weight-sensitive applications such as UAV, so the linear TE structure is a promising design improving of power generation while ensuring stronger bonding between the linear TEG and the walls of a combustion chamber of an engine.

Let us now turn to the thermomechanical stress issue associated with the integrated linear TEG into the walls of combustion chamber made of Fe-SMA. To this end, we made FEM analysis by using four different 2D geometries of TEG, (a) π TEG interfaced with planar AlN and Fe-SMA plates, (b) linear TEG with AlN and T-shaped Cu electrode interfaced with planar Fe-SMA plate, (c) linear TEG with dovetail-shaped AlN–Cu composite electrode, interfaced with planar Fe-SMA plate and (d) the present linear TEG with dovetailed-shaped AlN–Cu composite electrode interfaced with grooved Fe-SMA shrink-fit bonding. Fig. 7 shows the illustrated figures of four TEG designs, and the common conditions used for the FEM analysis were as follows: (1) element type: plane223, (2) mesh size: 0.25 mm square, (3) temperature boundary conditions: $T_H = 525$ °C and $T_C = 25$ °C for $\Delta T = 500$ °C, and (4) adiabatic environment to ensure complete 1-D heat flow. The compression of 0.7 MPa in horizontal direction was applied to linear TEG to minimize contact resistances thermally and electrically, which is generated by bolt-jointing. The maximum shear stress of the segmented π-shaped TEG shown in Fig. 7(a) is 759 MPa at the interface between AlN plate and Cu electrodes mainly due to a mismatch of
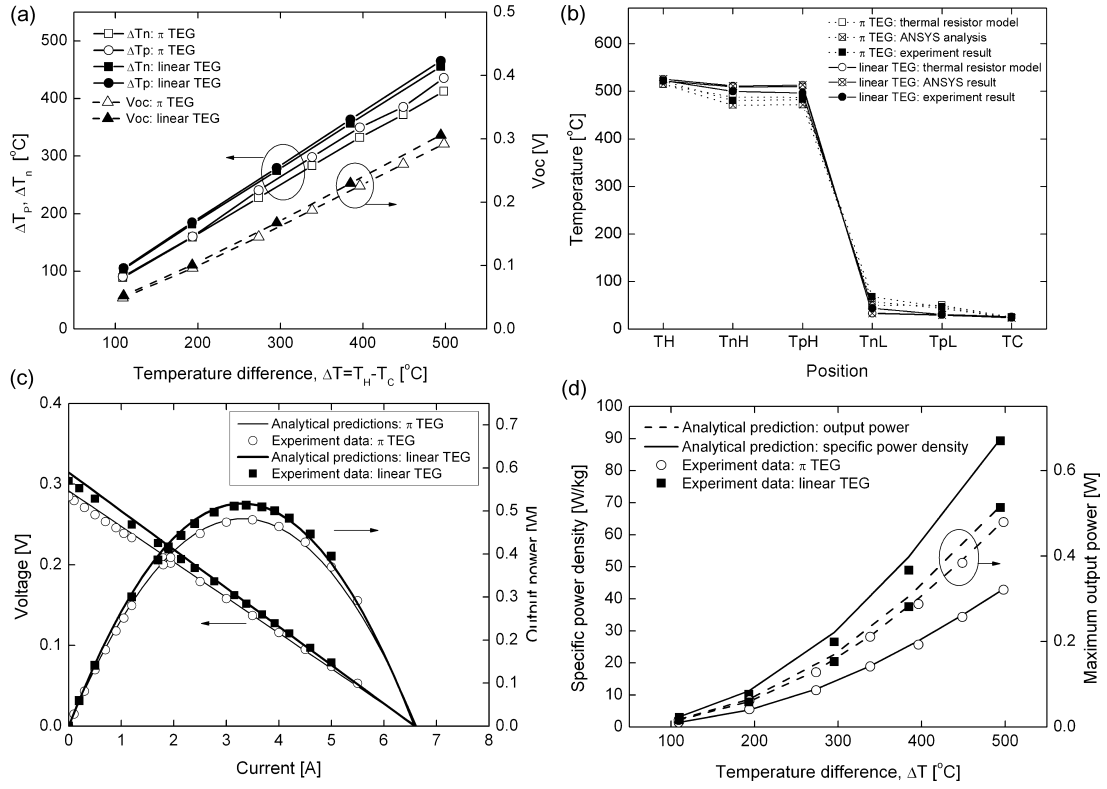
Fig. 6. Comparison of the linear TEG with π-shaped TEG: (a) temperature difference generated through only TE legs and V_{OC} as a function of ΔTs, (b) temperature profile of experiment data, ANSYS analysis and thermal resistor network model, (c) I–V curve and output power, and (d) the maximum output power and the specific power density as a function of ΔTs.
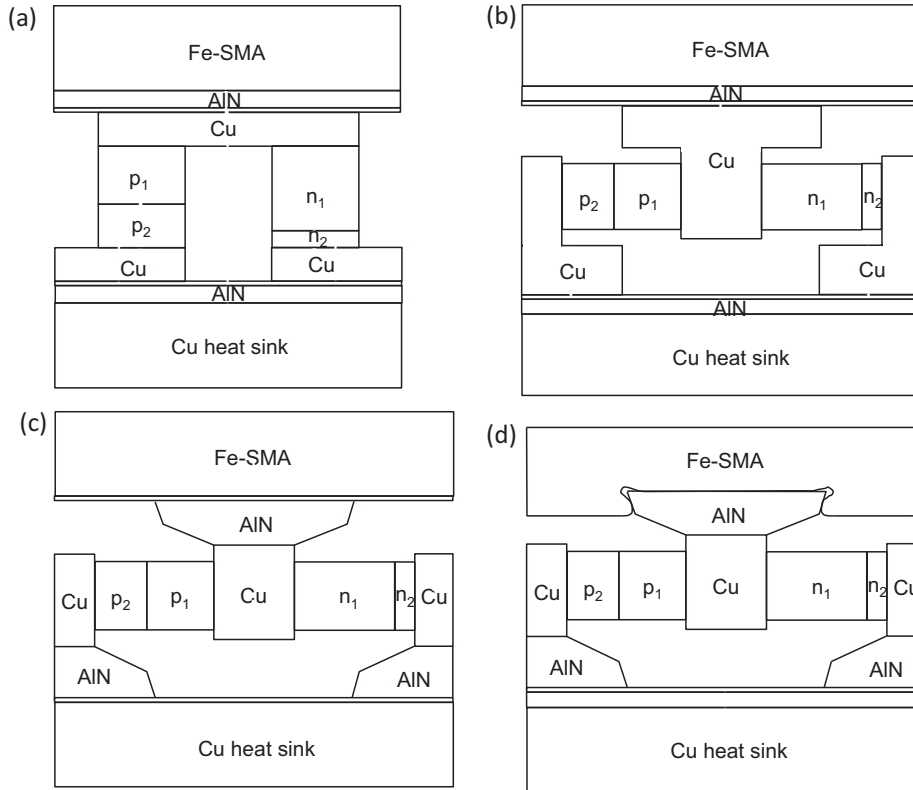

Fig. 7. The illustrative figures of four different TEG designs; (a) segmented π-shaped TEG, (b) segmented linear TEG using T-shaped solid Cu electrodes, (c) segmented linear TEG with dovetail-shaped electrodes using AlN–Cu composite interfaced with planar Fe-SMA plate, and (d) segmented linear TEG with dovetail-shaped AlN–Cu composite electrode using shrink-fitting integration to the grooved Fe-SMA plate.

Table 1
Comparison of various TEG designs: maximum shear stress, total weight of 1-pair assembly, and maximum temperature difference across TE materials.

TEG design	Max. shear stress	Total weight [g]	Max. temperature difference [°C]
(a)	759 MPa	5.6	446.9
(b)	1.3 GPa	4.7	439.3
(c)	439 MPa	2.9	423.3
(d)	402 MPa	2.9	458.9

coefficient of thermal expansion (CTE), and the maximum shear stress of the linear TEG design using bulk T-shape Cu electrode as shown in Fig. 7(b) occurred at AlN–Cu interface, which is 1.35 GPa. This indicates the linear TEG structure using solid T-shape electrode reported by Crane and Bell [12] and Sakamoto et al. [13] is weaker design than the above π-shaped TEG design. Regarding the linear TEGs using dovetailed AlN–Cu composite electrode, the maximum shear stress of 439 MPa occurred at the interface of Fe-SMA and AlN part in the TEG assembly without shrink-fitting, which is much lower than that of linear TEG using bulk Cu electrode in Fig. 7(b), and reduced by 42% compared with π-shaped TEG in Fig. 7(a). The linear TEG by using shrink-fit integration shown in Fig. 7(d) gives rise to the maximum shear stress of 402 MPa, which is reduced by 47% and 9% as compared with π-shaped TEG and linear TEG without shrink-fitting, respectively. As the top corners of the groove in Fe-SMA plate need modified to be rounded to eliminate stress concentration on the sharp part of assembled AlN, the maximum shear stress in the linear TEG design with shrink-fit design is reduced to the smallest. On the other hand, the conventional linear structure using a solid T-shape electrode, Fig. 7(b) was weak under high temperature environment due to larger thermal stress induced. Therefore, the FEA results based on the design shown in Fig. 7(a–d), we can conclude that the linear TEG with dovetailed AlN–Cu composite electrode built in the Fe-SMA based on shrink-fit bonding, is the best design among others. Table 1 summarizes each TEG design, as shown in Fig. 7(a–d). The total weight of the design (b) is estimated based on the measured weight of design (c) and (d) by replacing top AlN part with Cu block, where the weight of Fe-SMA is excluded. The design (a) generates the second largest temperature difference which is larger than that of the design (b) due to the thermal resistance of bulk T-shaped Cu electrode is higher than that of Cu planar electrode in the design (a). The design (c) has the smallest temperature gap because the thermal conductivity of the top AlN part is lower than that of Cu in the design (b). The design (d) of the lightest weight has the minimum shear stress and the largest temperature gap among others due to the shrink-fit joining method.

6. Conclusion

In this study, new TEG design is proposed, which is based on dovetail shaped AlN–Cu electrode built in the Fe-SMA plate by using shrink-fit bonding. This design gives rise to the best performance in terms of highest specific power density, while it is more robust and durable. The power output of the linear TEG is 7% higher than that of the π-shaped TEG. The specific power density of the linear TEG is dramatically increased from that of the π TEG, i.e., from 42.9 W/kg to 89.3 W/kg thank to lighter weight of the linear TEG, and the maximum shear stress of the linear TEG is reduced by 47% as compared with the conventional π-shaped TEG.

References

[1] H.J. Goldsmid, Thermoelectric Refrigeration, Plenum Press, New York, 1964.
[2] W.C. Hall, Terrestrial applications of thermoelectric generators, in: D.M. Rowe (Ed.), CRC Handbook of Thermoelectrics, CRC Press, Boca Raton, 1995.
[3] D.D. Pollock, Thermocouples: theory and properties, in: D.M. Rowe (Ed.), CRC Handbook of Thermoelectrics, CRC Press, Boca Raton, 1995.
[4] D.M. Rowe, Proc. Inst. Electr. Eng. 125 (1978) 1113–1136.
[5] J. Fleming, W. Ng, S. Ghamaty, Unmanned Aerospace Vehicles, Systems, Technologies, and Operations Conference and Workshop, Portsmouth, VA, 2002, AIAA 2002-3412.
[6] W.R. Pogue, N.J. Baucom, J.P. Thomas, M.A. Qidwai, Proceedings of AUVSI Unmanned Systems North America, Baltimore, MD, 2005.
[7] C. Yu, K.T. Chau, Energy Convers. Manage. 50 (2009) 1506–1512.
[8] T. Harman, J. Appl. Phys. 29 (1958).
[9] J. Schilz, L. Helmers, Y.S. Yang, Y. Noda, M. Niino, Proceedings of ICT97, Dresden, Germany, 1997, pp. 375–378.
[10] Y.S. Yang, M. Niino, A. Nishsida, J. Yoshino, Proceedings of ICT98, Nagoya, Japan, 1998, pp. 429–432.
[11] J.G. Stockholm, Large-scale cooling: integrated thermoelectric element technology, in: D.M. Rowe (Ed.), CRC Handbook of Thermoelectrics, CRC Press, Boca Raton, 1995.
[12] D.T. Crane, L.E. Bell, Proceedings of ICT06, Vienna, Austria, 2006, pp. 11–16.
[13] T. Sakamoto, T. Iida, Y. Taguchi, S. Kurosaki, Y. Hayatsu, K. Nishio, Y. Kogo, Y. Takanashi, J. Electron. Mater. 41 (2012) 1429–1435.
[14] H.S. Kim, Mechanical Engineering (Ph.D. dissertation), University of Washington, Seattle, 2013.
[15] M. Akasaka, T. Iida, A. Matsumoto, K. Yamanaka, Y. Takanashi, T. Imai, N. Hamada, J. Appl. Phys. 104 (2008) 013703–013708.
[16] T. Itoh, M. Yamada, J. Electron. Mater. 38 (2009) 925–929.
[17] H.S. Kim, W.S. Liu, K. Kikuchi, M. Taya, Proceedings of the 18th International Conference on Composite Materials, Jeju Island, South Korea, 2011.
[18] A. Sato, H. Kubo, T. Maruyama, Mater. Trans. 47 (2006) 571.
[19] T. Nemoto, T. Iida, J. Sato, T. Sakamoto, T. Nakajima, Y. Takanashi, J. Electron. Mater. 41 (2012) 1312–1316.
[20] B.W. Swanson, E.V. Somers, R.R. Heikes, J. Heat Transfer 83 (1961) 77–82.
[21] M.S. El-Genk, H.H. Saber, Energy Convers. Manage. 44 (2003) 1069–1088.
[22] M.S. El-Genk, H.H. Saber, Modeling and optimization of segmented thermoelectric generators for terrestrial and space applications, in: D.M. Rowe (Ed.), Thermoelectrics Handbook: Macro to Nano, CRC Press, Boca Raton, 2005.
[23] G. Min, D.M. Rowe, in: D.M. Rowe (Ed.), CRC Handbook of Thermoelectric, CRC Press, Boca Raton, 1995.
[24] M. Taya, Electronic Composites, Cambridge University Press, 2005.